

core, we find a line-of-sight velocity dispersion of $\sigma/(1+z) = 1300 \text{ km s}^{-1}$ for 19 objects, a very large value indeed. Thus finding an arc around such a massive and compact core would not be very surprising.

Pending the question of the reality of this feature, we believe that this class of cluster should receive high priority in a programme dedicated to the search for arcs. Will the object belong to the class of gravitational arcs? There are several classes of possible interlopers. The

most obvious are edge-on galaxies. Shells physically associated with certain cluster cores is a further possibility. Although the gravitational lens theory constrains the possible shapes of arc candidates, S-shaped features like the very well explained case in CI 0500-24 (Giraud et al., 1989) show that the range of possibilities is not so small. Finally, a difference in colour between the arc and the red cluster galaxies is not by itself convincing since a blue object can lie almost at any redshift.

References

Butcher H., Oemler, A., and Wells D.C., 1983, *Ap. J. Suppl.*, **52**, 183.
 Fort B., 1990, in *Gravitational Lensing*, Eds. Y. Mellier, B. Fort, and G. Soucail (Springer-Verlag), p. 221.
 Giraud E., Schneider P., and Wambsgans J., 1989, *The Messenger*, **56**, 62.
 Infante L., Pritchett C.J., and Quintana H., 1986, *A.J.*, **91**, 217.
 Petrosian V., Bergmann A.G., and Lynds R., 1990, in *Gravitational Lensing*, Eds. Y. Mellier, B. Fort, and G. Soucail (Springer-Verlag), p. 254.

Broadband Imaging Performance of IRAC with the New Philips 64 × 64 Array

A. MONETI, A. MOORWOOD, G. FINGER, M. MEYER and H. GEMPERLEIN, ESO

1. Introduction

IRAC, ESO's general-user Infrared Array Camera, has recently been upgraded with a new 64 × 64 array from Philips Components. A general description of IRAC can be found in *The Messenger* (**52**, 50; and **54**, 56). The new array was installed in IRAC and tested on the ESO/MPI 2.2-m telescope during two test runs, the first one in January and the second in March 1991. The first test run was aimed primarily at studying the capabilities of the new array in the L band. In between the two runs, the performance of the array was improved somewhat by decreasing the read-out noise and improving charge transfer efficiency, and during the second run capabilities of the array for deep imaging were investigated in more detail. Overall, the new array is considerably better than the 32 × 32 array that had been in use since November 1989, but, as will be shown, it falls short of expectations on several grounds.

2. The Philips 64 × 64 Array

The basic characteristics of the new array are summarized in Table 1. Note the low read-out noise (RON) of the new array. The RON could be even lower:

with a presumed preamplifier gain of $150e^-/ADU$ we were probably limited by the ADC resolution. Furthermore, in Section 6 we show that the actual gain may be as low as $100 e^-/ADU$, indicating a RON of $\leq 65e^-$ RMS.

Since the pixel size has not changed, the same magnifications are available (0.3, 0.5, 0.8, and 1.6"/pix) as previously. Detector response is linear at least up to half-full wells when illuminated by a uniform background.

A typical bias frame has about 20 bad pixels, but the number of bad pixels increases with detector integration time (DIT), indicating that these pixels have high dark current. We will therefore call them "hot" pixels. There are about 120 hot pixels in a DIT = 30 sec dark frame.

From each hot pixel a long streak extends upwards and a short one extends to the right. These streaks are very prominent on dark exposures, and become progressively less prominent as the incident background increases. The streaks are probably due to trapping effects in the read-out CCD, and we are experimenting with the CCD electronics to try to reduce the problem.

The mean bias level is stable within ~ 20 ADU. The precise level depends somewhat on the background level of

the previous frames, i.e. the array has some memory. This, however, is not a serious problem since (i) scientific observations are normally carried out in "beam switch" (b/s) mode, whereby a sky image is subtracted from the source image (the two images being acquired with the same integration time), and in the process the bias and the dark current are also subtracted; and (ii) flatfields have large enough signals that the uncertainty in the bias level is inconsequential.

3. Observations

During the first run, observations were carried out with both manual and automatic beam switching. In the latter mode, the telescope is moved automatically between the object position and a reference sky every 1–5 minutes. This mode was found to yield better quality data, and was subsequently used during the second run. Biases and flatfields were obtained throughout the runs, the latter were obtained on the day sky which provided a high signal in a short detector integration time (DIT), and hence flatfield frames with few hot pixels. The flatfields were then bias-subtracted and normalized to unity for use in data reduction.

Table 1: Array characteristics

Detector material	Hg:Cd:Te
Cutoff wavelength	$\sim 4.2 \mu\text{m}$
Read-out system	Buried channel CCD
Pixel size	$48 \mu\text{m}$
Read-out noise (RON)	$\leq 130e^-$ RMS
Dark current (at 49 K)	$\sim 300e^- \text{ sec}^{-1}$
Net detector quantum efficiency	$\sim 20\%$ at $2.2 \mu\text{m}$
Full well capacity	$9 \times 10^6 e^-$

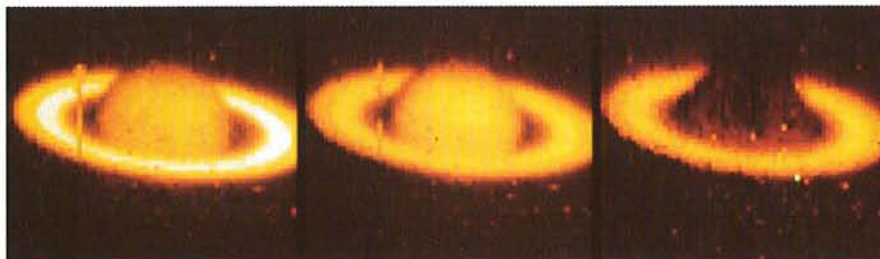


Figure 1: Saturn; from left to right: J, H, and K.

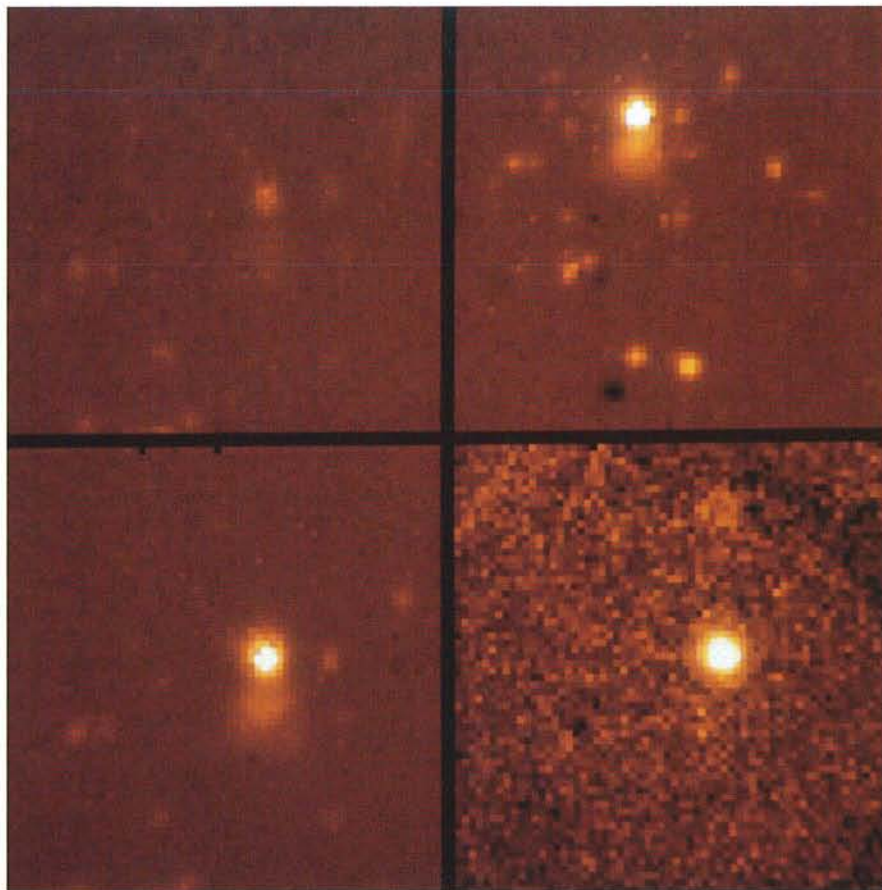


Figure 2: The star-forming region IRAS 08470-4321 in Vela, observed in stare mode. Top-left: H, 0.5''/pix; top right: K, 0.8''/pix; bottom-left: K, 0.5''/pix; and bottom-right: L, 0.5''/pix. Integration times were 5×60 sec at H and K, 64×1 sec at L. The brightest source has $K = 9.3^{\text{mag}}$ and $L = 7.2^{\text{mag}}$.

Table 2: Photometric Zero Points

Filter	Lens/Pixel scale			
	S1 1.6''	S2 0.8''	S3 0.5''	S4 0.3''
H			16.41(2)	
K	15.85(3)	15.85(3)	15.76(6)	15.50 (5)
L				14.52

Several images are presented in the Figures 1–4; details are in the captions. All images are shown with north to the top and east to the left. DITs of order 10–60 sec were used for the J, H, and K observations, while DITs of order 1 sec were used at L. Because of the large sky background, observations at L are not possible with pixel scales of 0.8'' and larger. Total integration times ranged

from a few to a few tens of minutes. All images were sky subtracted and flat-fielded, and the remaining bad pixels were “fixed” by careful median filtering.

4. Photometric Accuracy

Photometric standard stars from the list of Bouchet et al. (1991, AA, in press) were observed throughout the runs.

Table 3: Net system efficiencies

Filter/Lens	FDZM ¹ $\text{W cm}^{-2} \mu\text{m}^{-1}$	η_{NEW} %	η_{OLD} %
H/S3	1.19×10^{-13}	5.9	6.2
K/S3	4.12×10^{-14}	6.3	3.3
L/S4	5.40×10^{-15}	4.9	–

¹Flux density for 0 mag star.

During the first run we noted that in the J, H, and K bands, bright stars observed with short DITs showed streaks similar to the ones associated with the hot pixels, with an unknown amount of signal lost in the streak. These data did not yield reliable calibration. During the second run, we therefore chose fainter standard stars (i.e. 7th magnitude), for which DITs of order 20 sec is appropriate, in order to integrate enough background to overcome the streaking. Unfortunately the J-band sky emission is so low that this technique was not totally satisfactory in that band, and we will not present calibration data for it. On the other hand, no streaking occurs in the L band, where the thermal background is always very high.

From the observations of the standard stars, nominal photometric zero points (ZPs) were obtained; these are summarized in Table 2, where the uncertainty in the last decimal is given in parentheses. At L we observed only with lens S4, and only one standard star was observed so that no estimate of the uncertainty is available there. Table 2 is only partially complete, but it does show the accuracy with which the ZPs can be determined: overall, an uncertainty of $\leq 0.05^{\text{mag}}$ can be achieved.

5. Net System Efficiency

The observations of the standard stars were also used to determine the net (atmosphere + telescope + instrument) system efficiencies. The results are summarized in Table 3, where they are also compared to the old 32×32 Philips array. The nearly double efficiency at K results from a full coverage of that band. These numbers, however, are disappointing: with some reasonable assumptions for the atmospheric transmission, reflectivity of the telescope mirrors, and absorption by optical components within the camera, a net detector efficiency $\eta_{\text{d}} \approx 20\%$ at K is deduced.

6. Noise

When averaging together many observations of a given DIT, the IRAC acquisition software includes an option to calculate a noise frame that is stored together with the data. This frame has, for each pixel, the RMS variation determined from the individual read-outs. This option was used to measure the RMS noise under different background conditions and with different integration times. The noise was measured on parts of the array that are free of bad pixels, and hence these measurements reflect the behaviour of the good pixels. A plot of the measured noise as a function of

the incident signal is shown in Figure 5. The horizontal line denotes the noise floor, i.e. the RON, while the diagonal line denotes the expected shot noise. There are two possible interpretations for the offset between the measured and the expected noise: (i) there is some excess noise in the system whose origin is unknown at present; and (ii) the preamplifier gain was overestimated, and the true value is closer to $100e^-/ADU$. As a line through the measured points appears to be parallel to the expected line, the latter seems more likely. Should this be the case, the net detector efficiency would be correspondingly lower (i.e. $\sim 13\%$), as would the net efficiencies in Table 3.

7. Limiting Performance

In actual performance the noise that counts is the pixel-to-pixel noise in regions of the reduced image that contain pure sky. The improper subtraction of the bad pixels and of their streaks introduces a spatial noise which turns out to be the limiting factor under most conditions. Only at L, where the background is high enough that the streaking is totally overcome, is background limited performance achieved, though even there the odd bad pixel falling on top of the source of interest can seriously affect its measurement.

The pixel-to-pixel sky noise was measured on good parts of some reduced deep (e.g. 1 hour total integration time) frames, and from these measurements the limiting sensitivity was determined. These are summarized in Table 4 which gives both the background noise level ($1\sigma/\text{sec}/\text{pix}$) and the point-source sensitivity ($5\sigma/\text{sec}/\text{synthetic beam}$). The latter was determined for a pixel size of $0.5''$ and an equivalent beam diameter of $4''$, resulting in a beam area of 50 pixels. The measured sky brightness per arcsecond square (rather than per pixel) is also listed in Table 4. These are about 3 times larger than expected; about half of the excess can be ascribed to the oversized pupil stop which we hope to replace soon with a correctly sized one. The source of the remaining excess is not known at this time.

8. Conclusions

The results of the first runs of IRAC with the new Philips 64×64 array have been presented. This array is clearly better than the previous one, the main improvements being (a) larger size, (b) broader wavelength coverage, (c) better overall stability, (d) fewer bad pixels, and especially (e) lower read-out noise. There are several respects, however, in which the new array is disappointing: (a)

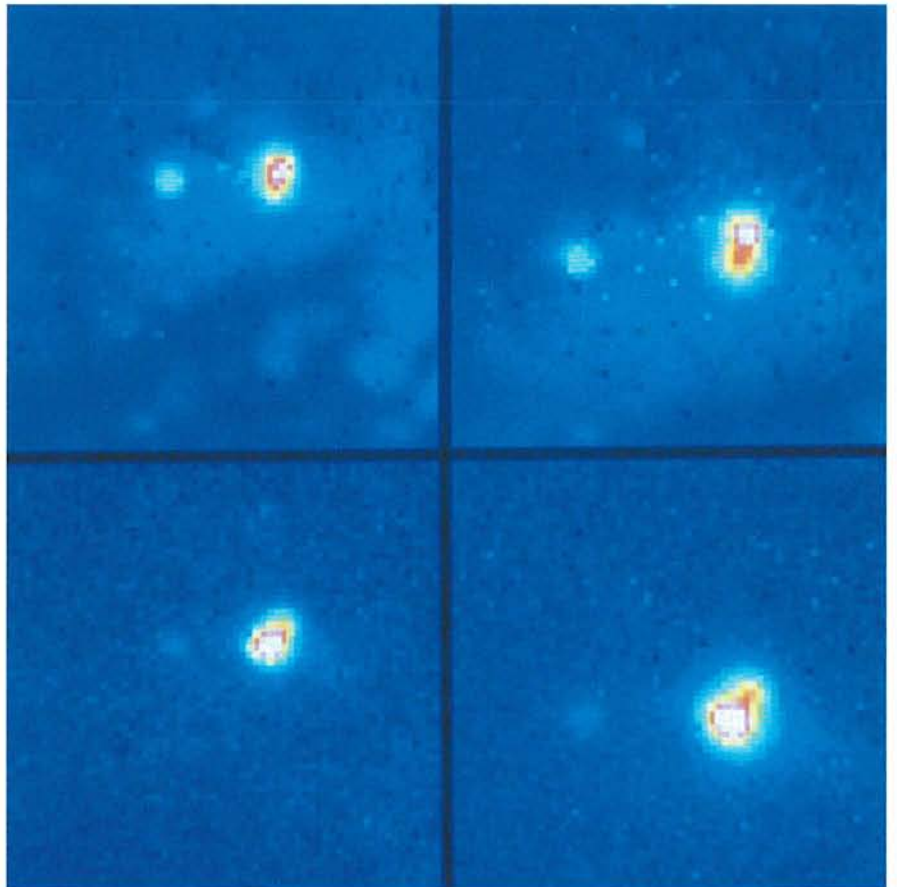


Figure 3: The infrared source in RCW 57, observed in b/s mode. Top-left: K $0.5''/\text{pix}$; top-right: K, $0.3''/\text{pix}$; bottom-left: L, $0.5''/\text{pix}$; and bottom-right: L, $0.3''/\text{pix}$. From the S4 images the following photometry was derived: *irs1-NW*: K = 8.4^{mag} and L = 4.9^{mag} ; *irs1-SE*: K = 8.8^{mag} and L = 4.3^{mag} .

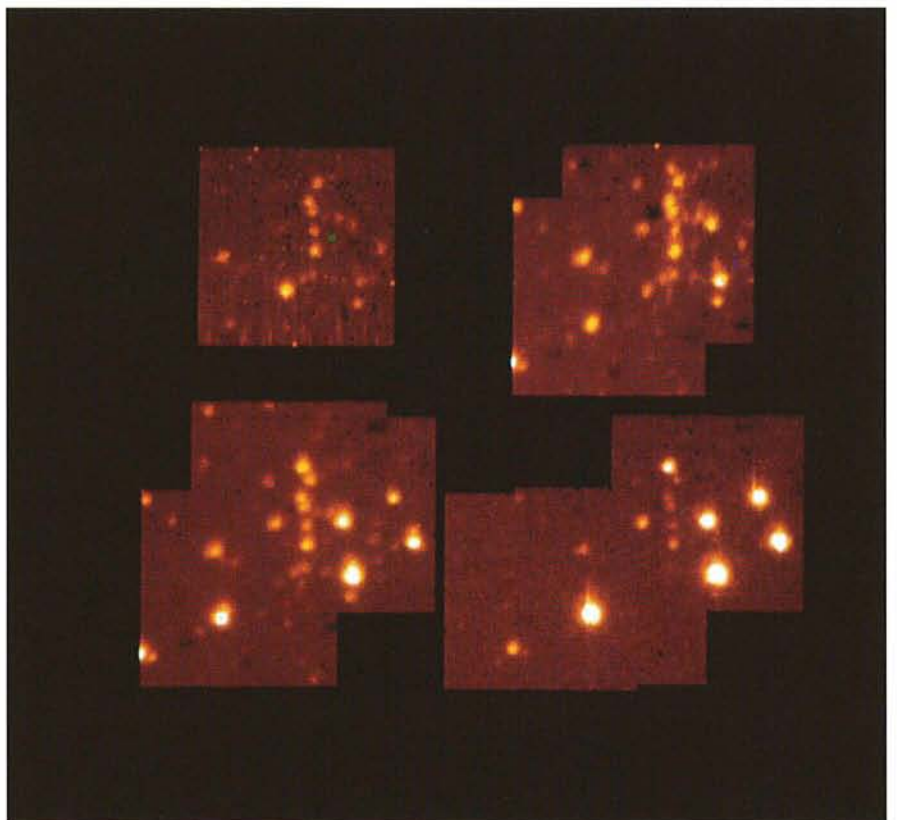


Figure 4: The cluster associated with IRAS 17430-2848, near the Galactic centre, observed in b/s mode at $0.3''/\text{pix}$. Top-left: J; top right: H; bottom-left: K; and bottom-right: L. A single frame was obtained at J, while a mosaic of several is presented at H, K, and L. The faintest objects at L are 9.8^{mag} .

the net detector quantum efficiency is low, (b) the number of bad pixels is a function of detector integration time, and (c) the streaking effect. The limits in actual performance are imposed by improper subtraction of the bad pixels and of their streaks. The combination of these problems makes the new array unsuitable for work under low background conditions, e.g. in the J band, in the H and K bands when working at high spatial resolution, with the 1.5–2.5 μm CVF and eventually with a Fabry-Perot etalon.

Under high background conditions (K at low spatial resolution and L), where there is sufficient sky background to overcome most of the streaking problem, good results can be obtained. Here one is limited by (a) improper subtraction of the first few pixels of the streaks from the hot pixels, which add noise to the sky background, and (b) the source of interest falling on a bad pixel, thus increasing the uncertainty in the photometry.

Table 4: Limiting sensitivities

Filter	Sky (mag/sq. arcsec)	1 σ /pix	5 σ /beam
H	12.8	19.5	15.6
K	10.7	19.5	15.6
L	1.7	14.2	10.3

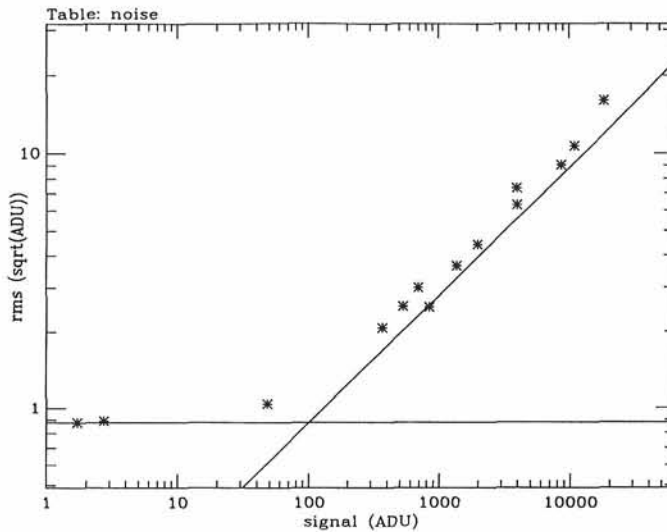


Figure 5: Measured RMS noise vs. signal. The horizontal line indicates the RON, and the diagonal line shows the expected noise for background limited performance.

Photographic Astronomy with MAMA

J. GUIBERT and O. MOREAU, Centre d'Analyse des Images, Observatoire de Paris, France

MAMA (Machine Automatique à Mesurer pour l'Astronomie) is a fast and accurate multichannel microdensitometer developed and operated by INSU and located at Observatoire de Paris. MAMA processes in a few hours photographic plates up to 14' \times 14' with a positional accuracy of 1 μm (repeatability: 0.2 μm) and a photometric accuracy of 2 per cent over a dynamical range of 3 densities. The detector is a RETICON CCPD array with 1024 photodiodes. The plate can be digitized either in a systematic way by lanes 10.24 mm wide, or in a random access mode from a catalogue of preliminary positions. The basic

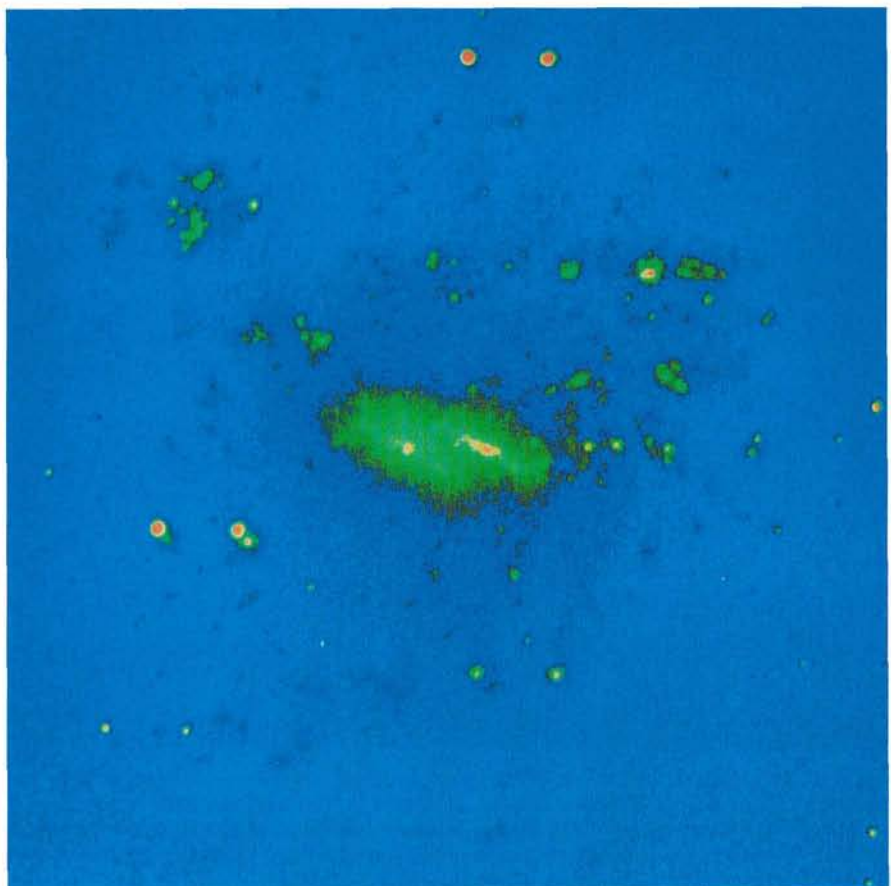


Figure 1: Detection of at least three regions with intense star formation in a spiral galaxy. A combination of two exposures with the 1-metre ESO Schmidt telescope on IIIa-F emulsion: UV (80 min. behind a UG 1 filtre) and R (25 min. behind a RG 630 filtre). The upper images belong to the R exposure and the lower to the UV exposure; the offset is 30''. It can be seen that the lower (southern) UV images of the star-forming regions are significantly brighter than the R images. Digitized with MAMA for a programme conducted by G. Comte (Observatoire de Marseille). Plate 7922 obtained on March 13, 1989.